Detecting Biosignatures in Nearby Rocky Exoplanets Using High-contrast Imaging and Medium-resolution Spectroscopy with the Extremely Large Telescope

Huihao Zhang , Ji Wang (王吉) , and Michael K. Plummer
Department of Astronomy, The Ohio State University, 140 W. 18th Ave., Columbus, OH 43210, USA; zhang.12043@buckeyemail.osu.edu
Received 2023 August 29; revised 2023 November 14; accepted 2023 November 22; published 2023 December 28

Abstract

In the upcoming decades, one of the primary objectives in exoplanet science is to search for habitable planets and signs of extraterrestrial life in the Universe. Signs of life can be indicated by thermal-dynamical imbalance in terrestrial planet atmospheres. O_2 and CH_4 in the modern Earth's atmosphere are such signs, commonly termed biosignatures. These biosignatures in exoplanetary atmospheres can potentially be detectable through high-contrast imaging instruments on future extremely large telescopes. To quantify the signal-to-noise ratio (S/N) with extremely large telescopes, we select up to 10 nearby rocky planets and simulate medium-resolution ($R \sim 1000$) direct imaging of these planets using the Mid-infrared ELT Imager and Spectrograph (ELT/METIS, 3–5.6 μm) and the High Angular Resolution Monolithic Optical and Near-infrared Integral field spectrograph (ELT/HARMONI, 0.5–2.45 μm). We calculate the S/N for the detection of biosignatures including CH_4, O_2, H_2O, and CO_2. Our results show that GJ 887 b has the highest detection of S/N for biosignatures, and Proxima Cen b exhibits the only detectable CO_2 among the targets for ELT/METIS direct imaging. We also investigate the TRAPPIST-1 system, the archetype of nearby transiting rocky planet systems, and compare the biosignature detection of transit spectroscopy with JWST versus direct spectroscopy with ELT/HARMONI. Our findings indicate JWST is more suitable for detecting and characterizing the atmospheres of transiting planet systems such as TRAPPIST-1 that are relatively further away and have smaller angular separations than more nearby nontransiting planets.

Unified Astronomy Thesaurus concepts: Direct imaging (387); Exoplanet atmospheric composition (2021); Biosignatures (2018); Extrasolar rocky planets (511)

1. Introduction

The question of whether life exists beyond Earth has been debated since Aristotle. We will perhaps have the opportunity to answer this question in the coming decades. The Astro2020 Decadal Survey (The National Academies of Sciences Engineering Medicine 2021) emphasizes the search for habitable worlds and extraterrestrial life as one of primary goals for the next decade. In addition, a series of high-performance extremely large telescopes are scheduled to come online (Gilmozzi & Spyromilio 2007; Sanders 2013; Roberge & Moustakas 2018). These extremely large telescopes will be vital in searching for the signs of life.

Evidence of life can be reflected in the thermal-dynamical imbalance of planetary atmospheres, which is manifested in certain molecular combinations in planetary atmospheres (Krissansen-Totton et al. 2018; Schwieterman et al. 2018). These molecular combinations are referred to as biosignature pairs. For example, the thermal-dynamical imbalance leads to the existing combination of O_2 and CH_4 in the atmosphere of Earth (Stüeken et al. 2020; Crouse et al. 2021).

Transit spectroscopy can be used to detect and characterize the atmosphere of transiting planets (Charbonneau et al. 2002; Deming et al. 2013; JWST Transiting Exoplanet Community Early Release Science Team et al. 2023). However, transit spectroscopy has limitations in detecting the atmospheres of nearby planets because of the low transit probability for these exoplanets (Mâlin et al. 2023). Direct imaging can overcome the problem of low transit probability and therefore effectively characterize both transiting and nontransiting planets (Werber et al. 2023) while obtaining atmospheric and orbital data (Wang & Jurgenson 2020).

Direct imaging faces challenges in separating the planetary signal from the noise due to the high contrast and small angular separation between the planet and the host star (Mawet et al. 2022). Currently, most of the known directly imaged exoplanets (Marois et al. 2008, 2010; Lagrange et al. 2010; Rameau et al. 2013; Macintosh et al. 2015; Chauvin et al. 2017) are around young host stars (<100 Myr) because the planet–star flux ratio (hereafter called "contrast") is higher due to the young planet's preservation of a large amount of heat during planetary formation (Fortney et al. 2008; Werber et al. 2023).

The challenges associated with small angular separation and high contrast in direct imaging can be addressed by future extremely large telescopes such as the European ELT (Gilmozzi & Spyromilio 2007), Thirty Meter Telescope (TMT; Sanders 2013), and Giant Magellan Telescope (GMT; Johns 2006). For example, the coronagraphs in the Mid-infrared ELT Imager and Spectrograph (ELT/METIS; Brandl et al. 2016) and High Angular Resolution Monolithic Optical and Near-infrared Integral field spectrograph (ELT/HAR-MONI; Jocou et al. 2022) enable the capability of medium-resolution (1000–5000) spectroscopy in the near-infrared (NIR) and mid-infrared (MIR) bands for high-contrast exoplanets (Quanz et al. 2015; Brandl et al. 2016; Wang et al. 2017; Carlomagno et al. 2020; Bowens et al. 2021). Werber et al. (2023) explore the ELT's ability to directly image habitable

Table 1
A List of Candidate Planets that Are Suitable for Direct Imaging with ELT

Planet	M_P ($M_\oplus$)	R_P ($R_\oplus$)	SMA (au)	D (pc)	$R_\star$ ($R_\odot$)	$\log(g)_\star$ (cm s^{-2})	$T_\star$ (K)	T_{eq} (K)	λ_{max} (μm)
GJ 1002 c	1.36	1.09	0.074	4.849	0.14	5.100	3024	182	2.90
GJ 1061 d	1.64	1.15	0.054	3.673	0.16	5.160	2953	224	2.80
GJ 1002 b	1.08	1.02	0.046	4.849	0.14	5.100	3024	231	1.80
Wolf 1061 b	1.91	1.20	0.038	4.306	0.31	4.900	3342	424	1.66
GJ 1061 c	1.74	1.17	0.035	3.673	0.16	5.160	2953	278	1.82
GJ 667 C c	3.80	1.82	0.125	7.244	0.33	4.690	3350	240	3.29
GJ 682 b	4.40	1.98	0.080	5.007	0.30	4.930	3028	259	3.04
GJ 887 b	4.20	1.93	0.068	3.290	0.47	4.780	3688	468	3.94
Proxima b	1.07	1.02	0.049	1.301	0.14	5.160	2900	217	7.11
Wolf 1061 c	3.41	1.71	0.089	4.306	0.31	4.900	3342	275	3.94

Note. All planets are suitable planets for ELT/HARMONI; planets in bold are suitable planets for ELT/METIS. M_P: mass of planet; R_P: radius of planet; SMA: semimajor axis of planet; D: distance between planet and Earth; $R_\star$: radius of star; $\log(g)_\star$: surface gravity of star; $T_\star$: surface temperature of star; T_{eq}: equilibrium temperature of planet; λ_{max}: maximum observable wavelength such that planet–star separation is larger than λ/D.

exoplanets and highlight the MIR band as the most suitable for direct imaging because planets have more favorable contrast in the MIR (Kasper et al. 2017).

However, exploration of direct imaging by extremely large telescopes in the NIR band remains valuable. Compared to MIR, NIR also has strong absorption features of gas (Wang et al. 2017) and offers a low sky background, as well as high spatial resolution, which may make it easier to detect exoplanets with small angular separation, such as those around M stars.

In this study, we use ELT/METIS (Brandl et al. 2008) in 3.0–5.6 μm and ELT/HARMONI (Kosmalski et al. 2016) in 0.5–2.45 μm as examples to explore and quantify the ability of extremely large telescopes to perform medium-resolution, high-contrast direct imaging of nearby known rocky exoplanets, using the methods of Wang et al. (2017) and Phillips et al. (2021). Our goal is to provide a ranking of the signal-to-noise ratio (S/N) of the biosignatures in the atmosphere of rocky exoplanets for ELT/METIS and ELT/HARMONI at different starlight suppression levels. We will also conduct a comparative study for the TRAPPIST-1 system using both the transit method with JWST and direct imaging with ELT/HARMONI.

In Section 2, we discuss the selection of candidate planets and instruments. In Section 3, we discuss the methods used to simulate and quantify the S/N of ELT, as well as the selection of planetary template atmospheres. In Section 4, we simulate direct imaging of planetary atmospheres using ELT/METIS and ELT/HARMONI. We quantify the S/N of the candidate planets. We then investigate the S/N of ELT/METIS and ELT/HARMONI for the atmosphere of the most ideal candidate planets under multiple instrument contrast levels. In Section 5, we discuss the S/N of biosignature pairs and compare the detection of biosignatures in exoplanet atmospheres by ELT and JWST. We summarize our results and draw conclusions on our study in Section 6. We also introduce our publicly available Python code on Zenodo (Zhang 2023).

2. The Selection of Planets and Instruments

2.1. The Selection of Candidate Planets

In this section, we select 10 and 5 temperate rocky planets from the NASA Exoplanet Archive (NEA)[1] and describe them

---

in Table 1, catering to ELT/HARMONI and ELT/METIS, respectively. Angular separation and low contrast are key parameters when selecting planetary targets for direct imaging. We employ NEA and the following selection criteria for ELT/HARMONI and ELT/METIS: (1) decl. below 0°, (2) top 10 planets with separations larger than the resolution for ELT/HARMONI (2.36 mas) at 0.45 μm and 5 planets with separations larger than the angular resolution for ELT/METIS (15.74 mas) at 3 μm, (3) contrast above 10^{-7}, (4) planets with radii between 1.0 and 2 $R_\oplus$, and (5) equilibrium temperature below 647 K. Based on these selection criteria, we select 10 and 5 planets, which are shown in Figure 1. Below, we detail how each of the criteria is being set.

2.1.1. Selection Criteria

We choose stars with declinations below 0° because they are more likely to be observable at the location of the ELT (the Southern Hemisphere; Tamai et al. 2016).

Angular separation limits of 2.36 and 15.74 mas are selected based on the ELT's spatial resolution (λ/D) computed with a 39.3 m diameter and the minimum working wavelength of ELT/HARMONI (0.45 μm) and ELT/METIS (3 μm).

We calculate the planet–star angular separation according to the reported semimajor axis and the distance from Earth.

Based on Wang & Jurgenson (2020), the planet contrast ϵ is calculated as follows:

$$\epsilon = \left(\frac{R_p^2}{a^2}\right) \cdot A, \tag{1}$$

where R_p is the planetary radius, a is the semimajor axis, and A is the planetary albedo. We adopt a uniform albedo value of $A = 0.3$ for all planets. This is the average albedo of Earth (Goode et al. 2001).

For R_p, we use values from NEA when available. In cases where the planetary radius is unknown, we utilize the mass–radius relation presented in Chen & Kipping (2017) to estimate the planetary radii with mass (or $m \sin i$). For planets detected through the radial velocity method, we assumed an edge-on orbit inclination (i) of 90°. Planets will have a larger mass and radius if $i \neq 90°$; in this scenario, the S/N of the planet is higher due to the larger radius, which results in a lower planet–star contrast.
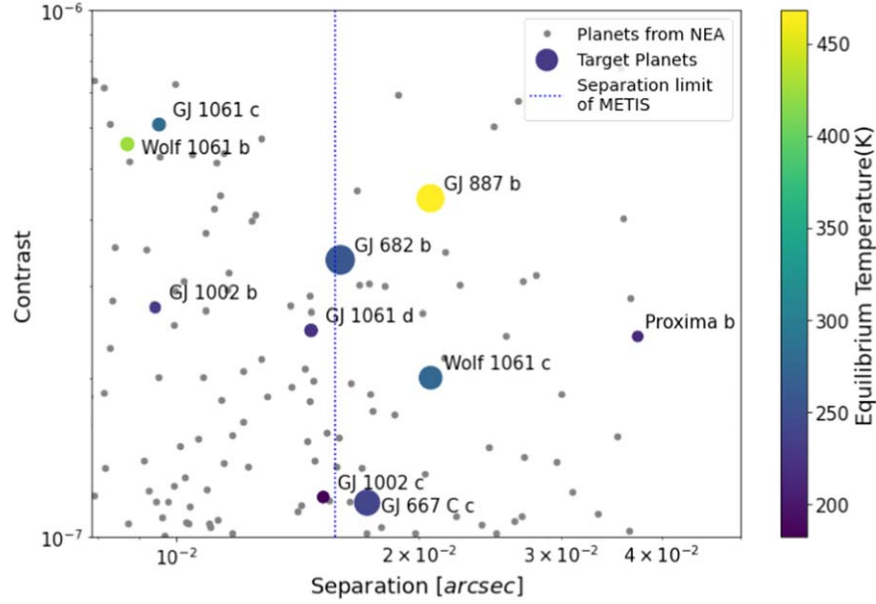
Figure 1. We select 10 and 5 candidate planets around nearby stars for ELT/HARMONI and ELT/METIS, respectively. As the spatial resolution of ELT/HARMONI is smaller than the plotting range, we only show the spatial resolution for ELT/METIS as the vertical dotted blue line. Planets located to the right of the dotted line are suitable planets for ELT/METIS. All colored points are suitable planets for ELT/HARMONI. The size of the colored point is proportional to the planet radius. The color of the point is based on the equilibrium temperature. All colored data points are the candidate planets listed in Table 1. Selection criteria can be found in Section 2.1. The gray points are other exoplanets from NEA that are less suitable for direct imaging with ELT.

We choose planets with radii between 1 and 2 $R_\oplus$ because they are more likely to have an Earth-like atmosphere, which is consistent with our choice of template spectra (Section 3.1.1). The imposed contrast limit of 10^{-7} is consistent with Wang & Jurgenson (2020).

A 647 K equilibrium temperature limit allows for the possibility of liquid water on the planetary surface (Selsis et al. 2007). We use equilibrium temperatures from NEA when available. For cases in which the equilibrium temperature is unknown, we use the following equation to calculate the equilibrium temperature T_{eq}:

$$T_{eq} = T_\star \sqrt{\frac{R_*}{2a}} (1 - A)^{1/4}, \qquad (2)$$

where $T_\star$ is the effective temperature of the star and R_* is the radius of the star.

2.1.2. Results of the Selection

We have identified 10 and 5 rocky exoplanets that meet the requirements for ELT/HARMONI and ELT/METIS, respectively, as shown in Figure 1. All of these planets are super-Earths detected through radial velocity. Based on their radii, these planets can be classified into two categories. The first category of planets has radii ranging from 1 to 1.20 $R_\oplus$. The second category of planets has radii between 1.70 and 2 $R_\oplus$.

Planets in the first category with smaller radii approximately equal to Earth's are thought to have lost their massive hydrogen envelopes. The hydrogen in the atmosphere is likely to be lost due to molecular photodissociation (Owen & Wu 2017) and/or core-powered mass loss (Ginzburg et al. 2016, 2018; Gupta & Schlichting 2019; Gupta et al. 2022; Owen & Schlichting 2023). Planets in this category are more likely to possess an Earth-like atmosphere due to their similar surface gravity. The first category of planets includes GJ 1002 c, GJ 1061 d,

Proxima b (or Proxima Cen b), GJ 1002 b, Wolf 1061 b, and GJ 1061 c.

For planets within the second category, not only is there a potential for the formation of an Earth-like atmosphere, but there also exists the likelihood of establishing a H-rich atmosphere (Miller-Ricci et al. 2009). Unlike the first type of planet, after the formation of the planetary core, due to a larger surface gravity, it is possible to retain hydrogen in the atmosphere. Under favorable conditions, these super-Earths are also deemed habitable (Haghighipour 2013; Seager 2013; Huang et al. 2022; Phillips et al. 2023). The second category of planets consists of GJ 667 C c, GJ 682 b, GJ 887 b, and Wolf 1061 c. We limit the scope of this work to the investigation of Earth-like atmospheres for both categories of planets.

2.2. The Selection of ELT Instruments

We chose to simulate biosignature detectability for ELT/METIS and ELT/HARMONI because both instruments possess the capability of high-contrast imaging with medium-resolution spectroscopy. The choice of medium resolution is due to our method being applicable to medium and low resolutions. The spatial bands covered by ELT/METIS (3–13 μm; Brandl et al. 2018) and ELT/HARMONI (0.47–2.45 μm; Thatte et al. 2016) coincide with our desired range of interest (0.5–5.6 μm). Both instruments are equipped with coronagraphs (Carlomagno et al. 2020; Jocou et al. 2022), possess medium-resolution imaging, and are cable of directly imaging exoplanets (Brandl et al. 2008, 2018; Kenworthy et al. 2016; Boccaletti 2018; Carlomagno et al. 2020; Houllé et al. 2021).

Among the known extremely large telescopes with high-contrast imaging capabilities, TMT/MODHIS (Mawet et al. 2022) was not selected due to its high spatial resolution ($R \sim 100,000$), while GMT/GMTIFS (Sharp et al. 2016) and ELT/MICADO (Davies et al. 2010) were not selected because their operating wavelengths (GMT/GMTIFS: 0.9–2.5 μm;
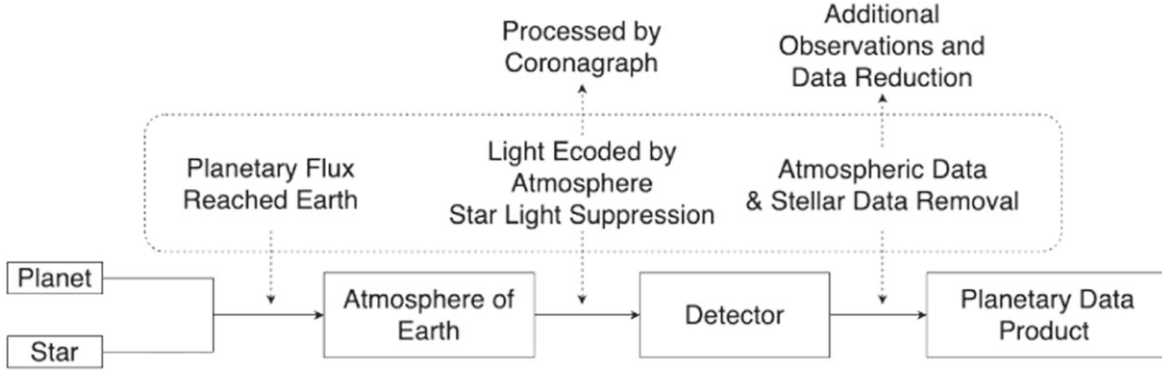
Figure 2. Flowchart outlining the simulation of ELT direct imaging applied to exoplanets. Photons from the star and planet pass through Earth's atmosphere and are processed by the coronagraph and captured by the detector. After obtaining the data, the effects of the atmosphere and star are removed through observations of the host star and the positions where no planet signals are received.

ELT/MICADO: 0.8–2.45 μm) are similar but narrower compared to ELT/HARMONI (0.47–2.45 μm).

3. Method

3.1. Simulating ELT Direct Imaging of Rocky Exoplanets

The flowchart in Figure 2 delineates the procedure and system-related inputs utilized in the simulation. Specifically, we perform an end-to-end calculation for the photon count at an ELT instrument. For the reflection light, the photon originates from the host star, is reflected by the planet and encoded by the planet's atmosphere, and then passes through the Earth's atmosphere, a telescope, and a high-contrast instrument before being recorded on a detector. For thermal emission, the only difference is that the photon originates from the planet.

We assume the spectral resolution of ELT/METIS to be 1000, which is consistent with the information provided by ESO.[2] We assume an instrument contrast of 10^{-4} for ELT/METIS, which is approximately the average postprocessing contrast for ELT/METIS within 0–4.7 λ/D (Carlomagno et al. 2016). We assume the instrument throughput η to be 0.1; this is a conservative assumption, because it was assumed to be 0.36 in Carlomagno et al. (2020).

For the resolution of ELT/HARMONI, we choose to use $R = 1000$ to compare to the ELT/METIS results, although the minimum resolution of ELT/HARMONI is 3500 (Thatte et al. 2016). While a slightly higher resolution would boost the detection S/N, the change from $R = 1000$ to 3500 is insignificant, as shown in Figure 16 in Wang et al. (2017). As ELT/HARMONI exhibits a raw contrast of 10^{-1} within low-separation angles (0–5 λ/D), we assume a postprocessing instrument contrast of 10^{-3} for ELT/HARMONI, which is consistent with the extent of contrast improvement achieved using postprocessing techniques with ELT/METIS (Carlomagno et al. 2016). As with ELT/METIS, we assume an instrument throughput η of 0.1 for ELT/HARMONI. Below, we detail how each of the steps in the flowchart is being simulated.

3.1.1. Simulating Exoplanet Spectra

Upon identifying suitable planets, we proceed to search for appropriate atmospheric models for the candidate planets. We

---
[2] https://elt.eso.org/instrument/METIS/

assume all candidate planets possess a modern Earth atmosphere with biosignatures: O_2, CO_2, CH_4, and H_2O. The molecular pairs O_2+CH_4 are widely considered as biosignatures in the atmosphere of modern Earth (Stüeken et al. 2020; Crouse et al. 2021). CH_4+CO_2 are biosignatures in the atmosphere of Archean Earth; considering their high detectability (Wogan et al. 2020), we also use them as biosignatures for this project. H_2O is generally considered as a prerequisite for sustaining life.

We use BT-Settl high-resolution synthetic spectra (Allard 2014) to simulate an M star, based on the stellar effective temperature, metallicity, and surface gravity. Assuming a star radius, $R_\star$, we can obtain the incident flux of the star ($F_\star$, units of W m^{-2}) at distance D with Equation (3):

$$F_\star = 10^{F_0(\lambda)-8} \cdot d\lambda \cdot \frac{R_\star^2}{D^2}, \qquad (3)$$

where $F_0(\lambda)$ is the spectral template's flux array, a dimensionless quantity. $d\lambda$ is the wavelength per resolution element, computed as λ_0/R, where λ_0 is the central wavelength and R is the spectral resolution.

We use SIMBAD (Wenger et al. 2000) photometry to check the validity of the BT-Settl spectra. Using TRAPPIST-1 as an example, we obtain R-, i-, Z-, J-, H-, K-, and W_1-band photometric data from SIMBAD (shown in Figure 3).

We calculate the incident flux of a BT-Settl spectrum with stellar parameters that best resemble TRAPPIST-1 (Table 2). The comparison results show that the flux difference between SIMBAD photometry and a BT-Settl spectrum can be as high as 83% but is predominantly within 25% for the 1–5 μm range in which we are mainly interested and the majority of planet signal comes from. We also selected five host stars (with $T_{\rm eff}$ from 2600 to 3700 K) of suitable planets to examine the difference between models and observations. The flux differences are all within 25% for the 1–5 μm range.

The planet flux (F_p) on Earth has two components, the reflection component (F_r) and the thermal emission component (F_t). F_r can be calculated via Equation (4):

$$F_r = F_\star \cdot A_g \frac{R_p^2}{4a^2}, \qquad (4)$$

where $F_\star$ is the stellar flux irradiating the planet and A_g is the wavelength-dependent albedo, as shown in Figure 8 in Wang
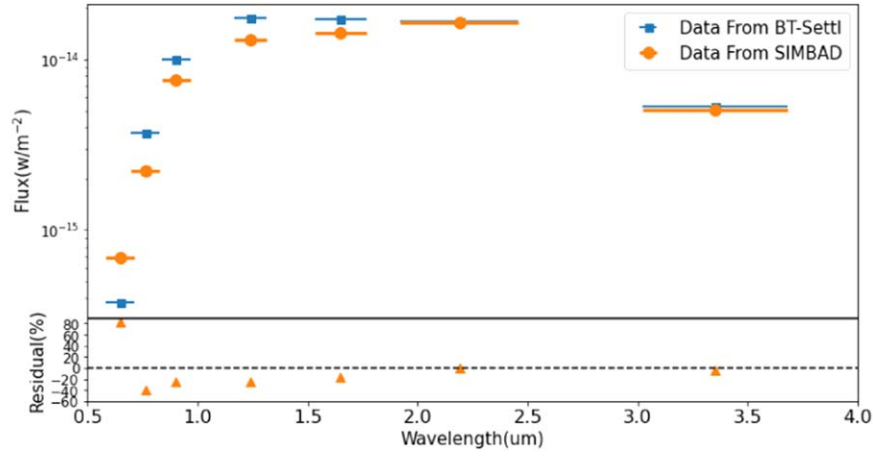
Figure 3. Top: flux of TRAPPIST-1 from SIMBAD vs. flux of TRAPPIST-1 from BT-Settl. Bottom: the residual between SIMBAD and BT-Settl in percent. For comparison, we choose data from the R, i, Z, J, H, K, and W_1 bands in SIMBAD.

et al. (2017). We employ A_g to simulate the reflected spectrum by the atmosphere of the planet.

The albedo spectra (A_g) for modern Earth used in our study were derived from a high-resolution model developed by Hu et al. (2012a, 2012b, 2013) and Hu & Seager (2014). This model calculates molecular abundances across different altitudes, incorporating the effects of photochemical and disequilibrium chemistry, with details in Hu et al. (2012a). Cloud impacts were included by averaging clear and high-cloud scenarios, resulting in a continuum albedo of 0.3, similar to the approach of Des Marais et al. (2002). The spectra, covering a wavelength range of 0.5–5.6 μm with a spectral resolution of $R = 500{,}000$, include opacities of major atmospheric components and are presented as scaled albedo values.

The thermal emission component F_t is calculated as follows:

$$F_t = F_b \cdot \bar{A}_g \cdot \theta, \qquad (5)$$

where F_b is the blackbody radiation of the planet, $\bar{A}_g$ is the normalized planet albedo spectrum, and θ is the extended solid angle of the planet as seen from Earth, which is $\frac{\pi R_p^2}{D^2}$.

3.1.2. Simulating Observations of ELT

After arriving on Earth, the light is encoded by the Earth's atmosphere, processed by the telescope and coronagraph, and recorded by a detector. We can calculate the flux received by the detector (F_{det}) via Equation (6):

$$F_{det} = \eta \cdot (F_p \cdot f_{tran} + F_\star \cdot f_{tran} \cdot C + F_{sky}), \qquad (6)$$

where F_p is the flux of the planet including its reflection and thermal components, $F_\star$ is the flux of the star on Earth, C is the instrument contrast (or level of starlight suppression), f_{tran} is the transmission of the sky, and F_{sky} is the emission flux of the sky. We use the ESO SkyCalc Tool (Noll et al. 2012; Jones et al. 2013) to model sky transmission and emission with an observatory altitude of 3060 m and an airmass of 1.5 for the model of the sky. In calculating sky emission, we use a wavelength of 1.5 μm for ELT/HARMONI and 4.3 μm for ELT/METIS, which is the central wavelength for the two instruments in this project.

The number of photons (N) recorded by the detector in each wavelength channel is calculated as follows:

$$N = \frac{F_{det} \cdot S \cdot t}{E}. \qquad (7)$$

F_{det} is the flux received by the detector, S is the area of the telescope for which we use 978 m^2, t is the exposure time, and E is the photon energy at the central wavelength of each spectral bin.

3.1.3. Reduced Spectrum

By the above steps, we can simulate the number of photons received by the detector during direct imaging of exoplanets. The separation of planet photons (N_p) from the photons received by the detector (N_{det}) can be achieved through additional observations.

N_{det} consist of three sources: (1) photons from the star encoded by the atmosphere and the coronagraph, $N_\star \cdot C \cdot f_{tran}$; (2) photons from sky emission, N_{sky}; and (3) photons from the planet encoded by the atmosphere, $N_p \cdot f_{tran}$.

The process of N_p separation can be described as follows: (1) $N_p' = N_{det} - (N_\star \cdot C \cdot f_{tran} + N_{sky})$, and (2) N_p'/f_{tran}, where $N_p' = N_p \cdot f_{tran}$.

$N_\star \cdot C \cdot f_{tran} + N_{sky}$ can be obtained through observations at locations where no planet signals are received. The transmission of the sky (f_{tran}) can be obtained through observations of a telluric standard star (Wang et al. 2017).

3.1.4. Noise

Based on the propagation uncertainty, we simulated the observational noise σ after separation as follows:

$$\sigma = \sqrt{\left(\frac{N_p \cdot \sigma_{f_{tran}}}{f_{tran}}\right)^2 + \frac{N_{det} + N_\star \cdot C \cdot f_{tran} + N_{sky}}{f_{tran}^2}}, \qquad (8)$$

where $N_\star \cdot C \cdot f_{tran}$ is the number of stellar photons received at the telescope. σ_{tran} is the uncertainty of sky transmission; here we assumed that $\sigma_{f_{tran}} = 0.001 \cdot f_{tran}$. The derivation of Equation (8) is described in Appendix A. We also assume a different fractional error at $\sigma_{f_{tran}} = 0.01 \cdot f_{tran}$, and the results are reported in Table 7 and discussed in Section 5.4.

Table 2
TRAPPIST-1 Parameters

	Radius ($R_\odot$)	Mass ($M_\odot$)	$T_{\rm eff}$ (K)	Metallicity (dex)	log g (cm s^{-2})	SMA (au)	D (pc)	$T_{\rm eq}$ (K)
TRAPPIST-1	0.1192	0.0898	2566	0.040	5.2396	⋯	12.1	⋯
TRAPPIST-1 e	0.920	0.692	⋯	⋯	⋯	0.029	⋯	228.5
TRAPPIST-1 h	0.755	0.326	⋯	⋯	⋯	0.0619	⋯	157.1

Note. All parameters we used are the latest NEA data.

3.2. Quantifying the Ability of ELT to Detect Biosignatures

After establishing the method for simulating ELT observation and various noise sources, we propose a method for quantifying the S/N for explanatory atmospheric gases. This S/N is quantified by the S/N of the gases in its observable feature wavelengths from the minimum working wavelength to $\lambda_{\max}$, where $\lambda_{\max}$ is calculated by equating the angular resolution (λ/D) to the planet–star separation. Above $\lambda_{\max}$, the angular resolution falls below the planet–star separation. Therefore, we consider the planet uncharacterizable above $\lambda_{\max}$. Below, we detail how each of the steps is being calculated or simulated.

3.2.1. S/N

We define the S/N for the gas in the atmospheres of exoplanets with Equation (9):

$$S/N = \frac{N' - N}{\sigma}, \qquad (9)$$

where N is the observed photon number for the planet. N and σ can be obtained through an ELT observational procedure as shown in Section 3.1. N' is the observed photon number for the planet, assuming the planet has a biosignature-free (no CO_2, CH_4, H_2O, or CO) modern Earth atmosphere. N' can be obtained through the same procedure as for N, with the only difference being that N' assumes the planet has a modern Earth atmosphere that lacks CH_4, CO_2, O_2, and H_2O.

To obtain a biosignature-free modern Earth atmosphere, we remove the absorption line of the CH_4, CO_2, O_2, and H_2O by finding the envelope of the albedo of modern Earth. To find the envelope, we divided the spectrum into 430 intervals, using the largest value in each interval to construct the envelope. Choosing TRAPPIST-1 e (the archetype of the nearby transiting terrestrial planet) as an example, the spectra of a biosignature-free atmosphere and the modern Earth atmosphere are shown in Figure 4.

3.2.2. Quantifying the S/N of the ELT Direct Imaging Planet Atmosphere

Building on the work of Phillips et al. (2021), we have developed a method to quantitatively evaluate the S/N of ELT for planetary atmospheric gases with Equation (10):

$$S/N_{\rm gas} = \sqrt{\sum_i S/N_i^2}, \qquad (10)$$

where $S/N_{\rm gas}$ is the S/N of gas in Equation (9), and i is the index for each feature wavelength as shown in Table 3.

We identify the feature wavelengths based on the albedo spectrum of modern Earth. The region where the albedo of a gas is all above 0.15 (half the albedo of the modern Earth) is

Table 3
Feature Wavelengths of Biosignature Gas We Set for Modern Earth Atmosphere

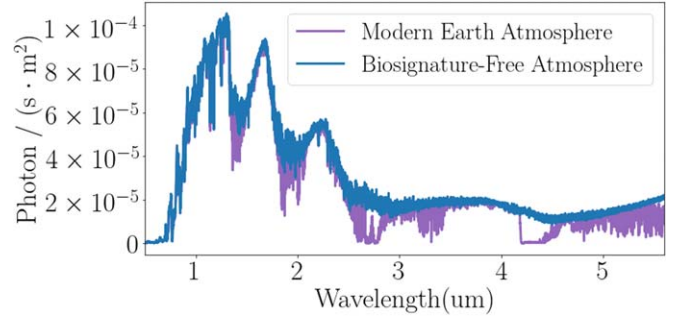| Feature Wavelength (μm)			
H₂O	CH₄	CO₂	O₂
0.90–0.91	1.64–1.68	1.57–1.59	0.62–0.63
0.93–0.97	2.18–2.38	1.60–1.61	0.68–0.69
1.11–1.16	3.88–3.41	1.99–2.09	0.76–0.77
1.31–1.32	3.41–3.71	4.17–4.51	1.25–1.28
1.33–1.43	3.79–3.82	⋯	⋯
1.45–1.50	3.88–3.92	⋯	⋯
1.76–1.94	3.98–3.99	⋯	⋯
1.97–1.98	⋯	⋯	⋯
2.41–2.45	⋯	⋯	⋯
3.00–3.16	⋯	⋯	⋯
4.62–4.63	⋯	⋯	⋯
4.66–4.69	⋯	⋯	⋯
4.95–5.16	⋯	⋯	⋯
5.27–5.60	⋯	⋯	⋯

Figure 4. TRAPPIST-1 e photon flux detected on Earth, assuming TRAPPIST-1 e has a biosignature-free and modern Earth atmosphere. The difference between the two curves is caused by biosignature gases. The greater the differences, the stronger the impact of gases on the observed spectrum, resulting in a higher S/N of gases. We assumed a spectral resolution of 1000.

considered to be the feature wavelength of that gas. The wavelengths where two or more gases have overlapping features will not be considered. Based on the assumed Earth atmosphere model (A_g), the feature wavelengths of each gas have been determined. These feature wavelengths are described in Table 3, shown in Figure 5.

For example, when calculating the S/N for ELT/HARMONI observations of Wolf 1061 b, the observable wavelengths are from 0.45 μm (minimum working wavelength for ELT/METIS) to $\lambda_{\max} - 1.66\,\mu$m (as shown in Table 1). The feature wavelengths of CO_2 are therefore 1.57–1.59 and 1.60–1.61 μm. The S/N of CO_2 can be quantified by summing up all of the S/Ns above two CO_2 wavelength regions using Equation (10). The S/N of the atmosphere will also be calculated through a similar process, with the difference being
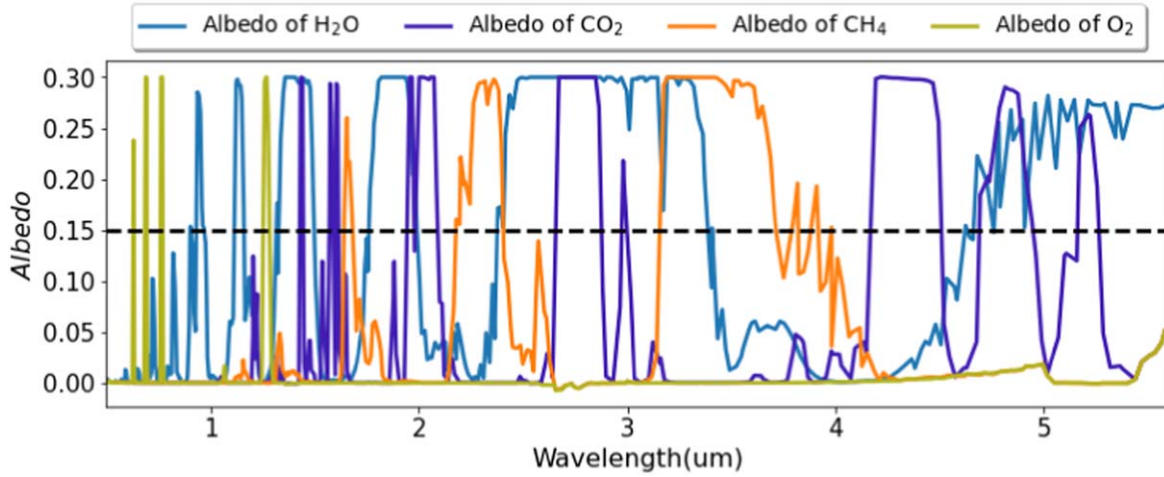
Figure 5. The albedos of H_2O, CO_2, CH_4, and O_2 in the atmosphere of modern Earth. The interval where the albedo of a gas exceeds 0.15 is considered as the feature wavelength for that gas. The black dashed line is the criterion for albedo of 0.15. The wavelengths where two or more gases have overlapping features will not be considered as feature wavelengths. The wavelengths of the intervals with albedos higher than 0.15 are described in Table 3.

Table 4
S/Ns of Biosignatures for Candidate Planets with ELT/METIS and ELT/HARMONI Direct Imaging

ELT/METIS						
Rank	Planet	S/N_{total}	S/N_{H_2O}	S/N_{CH_4}	S/N_{CO_2}	S/N_{O_2}	$T_{S/N=5}$(hr)
1	GJ 887 b	18.24	4.81	17.59	0.00	0.0	0.75
2	Proxima b	2.22	1.57	1.16	1.05	0.0	51
3	Wolf 1061 c	0.72	0.24	0.67	0.00	0.0	490
4	GJ 682 b	0.13	0.13	0.00	0.00	0.0	14300
5	GJ 667 C c	0.07	0.07	0.00	0.00	0.0	54500
ELT/HARMONI						
Rank	Planet	S/N_{total}	S/N_{H_2O}	S/N_{CH_4}	S/N_{CO_2}	S/N_{O_2}	$T_{S/N=5}$(hr)
1	GJ 887 b	4.94	3.18	2.74	2.40	1.02	10.5
2	Wolf 1061 b	1.04	0.94	0.12	0.20	0.37	235
3	Wolf 1061 c	0.64	0.43	0.34	0.29	0.13	625
4	Proxima b	0.49	0.39	0.23	0.19	0.09	1050
5	GJ 682 b	0.47	0.36	0.23	0.19	0.09	1150
6	GJ 1061 c	0.44	0.41	0.09	0.06	0.11	1300
7	GJ 667 C c	0.26	0.18	0.14	0.12	0.06	3800
8	GJ 1061 d	0.25	0.19	0.12	0.10	0.05	4000
9	GJ 1002 b	0.13	0.12	0.03	0.02	0.03	14500
10	GJ 1002 c	0.08	0.06	0.04	0.03	0.01	39000

Note. $T_{S/N=5}$(s): required exposure time to reach an S/N_{total} of 5. We assume an exposure time of 10 hr and a resolution of 1000 for ELT and a coronagraph contrast of 10^{-3} for ELT/HARMONI and 10^{-4} for ELT/METIS.

that the feature wavelength will be the merged feature wavelengths for all gases in the atmosphere up to λ_{max}.

4. Results

We applied the above method to the candidate planets and obtained observational results in the wavelength ranges of 0.5–2.45 μm for ELT/HARMONI and 3–5.6 μm for ELT/ METIS with 10 hr exposure times. Based on the observational results, we quantified and ranked the S/N of ELT/METIS and ELT/HARMONI for biosignatures in the atmosphere of the candidate planets, as shown in Table 4. The ranking indicates that GJ 887 b is the most suitable known planet for direct imaging of its atmosphere with ELT/METIS and ELT/ HARMONI, and Proxima b is the most suitable known planet for direct imaging of CO_2 with ELT/METIS.

Considering the diversity of instrument contrasts, we explored the S/N of ELT/METIS and ELT/HARMONI in the case of different instrument contrast (for ELT/METIS: 10^{-3}–10^{-6}; for ELT/HARMONI: 10^{-2}–10^{-5}); for the highest ranked target, GJ 887 b, as shown in Table 5. We conclude that the S/N of ELT/METIS and ELT/HARMONI will improve with the enhancement of the instrument contrast. Specifically, the enhancement of instrument contrast contributes most significantly to the improvement in the S/N of ELT/ HARMONI. We detail the results below.

4.1. ELT/METIS

We have quantified the S/N of ELT/METIS for direct imaging of exoplanet atmospheres within 3–5.6 μm. Based on the quantitative results, we present a ranking of candidate

Table 5
S/N of ELT/METIS and ELT/HARMONI for GJ 887 b

S/N of ELT/METIS for GJ 887 b					
C	H_2O	CH_4	CO_2	O_2	Total
10^{-3}	1.92	7.05	0	0	7.31
10^{-4}	**4.81**	**17.59**	**0**	**0**	**18.24**
10^{-5}	8.10	30.11	0	0	31.18
10^{-6}	9.58	36.57	0	0	37.81
S/N of ELT/HARMONI for GJ 887 b					
C	H_2O	CH_4	CO_2	O_2	Total
10^{-2}	1.00	0.86	0.76	0.32	1.56
10^{-3}	**3.18**	**2.74**	**2.40**	**1.02**	**4.94**
10^{-4}	10.05	8.66	7.60	3.22	15.62
10^{-5}	31.67	27.31	23.99	10.16	49.29

Note. C: instrument contrast. The bold rows are the data for the assumed contrast of this project.

planets in terms of their S/N. According to the ranking, we find that the three most detectable planets are GJ 887 b, Proxima b, and Wolf 1061 c, while the least detectable planet is GJ 667 C c. GJ 667 C c requires an exposure time of approximately 54,500 hr in order to achieve S/N = 5. With a 10 hr exposure time, the S/N of GJ 887 b far surpasses that of other planets, being approximately 8.2 times higher than that of Proxima b, 25.3 times higher than that of Wolf 1061 c, and approximately 140–260 times higher than the remaining planets.

The high S/N of GJ 887 b is reasonable due to its abundant reflection flux and thermal flux contributions. The abundant reflection flux and thermal flux in the planet are attributed to the high luminosity of its host star (the brightest red dwarf; Jeffers et al. 2020), as well as its small semimajor axis and large planetary radius. These conditions allow it to have a high equilibrium temperature and reflect a significant amount of light from the star.

In terms of gas S/N (or S/N_{gas}), we find that ELT/METIS has the capability to detect CO_2, CH_4, and H_2O in the NIR band but lacks the capability to detect O_2. At an exposure time of 10 hr, for planets with S/N > 5 (GJ 887 b), CH_4 exhibits the highest S/N, approximately 4 times stronger than that of H_2O, but CO_2 and O_2 are not detectable due to the observable wavelength (3–3.94 μm). For other planets, CO_2 is only detectable for Proxima b, and O_2 is not detectable for any of them, as the observable wavelengths do not include the feature wavelengths of CO_2 and O_2.

CO_2 is only observable for Proxima b with ELT/METIS due to its large angular separation. The angular separation of Proxima b allows its observable wavelengths for ELT/METIS to range from 3 to 7.11 μm (see λ_{max} in Table 1), which includes strong features of CO_2 from 4.17 to 4.51 μm (see Table 3). In contrast, the observable wavelengths for other planets with ELT/METIS are limited to within 4 μm, which does not cover the feature wavelengths of CO_2.

For the impact of instrument contrast on the S/N of ELT/METIS, from $C = 10^{-3}$ to 10^{-4}, 10^{-4} to 10^{-5}, and 10^{-5} to 10^{-6}, the S/N of ELT/METIS for GJ 887 b improves by 149.5%, 70.9%, and 21.3%, respectively. Once C reaches 10^{-5}, the enhancement of instrument contrast provides less aid to the performance of ELT/METIS. This is because the dominating noise source changes from stellar noise to sky background noise at higher contrast levels.

The range of contrast is chosen to be consistent with the expected contrast levels achievable with multiple postprocessing techniques at different angular separations (Carlomagno et al. 2016).

4.2. ELT/HARMONI

We have quantified the S/N of ELT/HARMONI within 0.5–2.45 μm. Based on the quantitative results, GJ 887 b remains the most detectable planet, while GJ 1002 c is the least detectable planet. For GJ 887 b (the planet with the highest S/N), ELT/HARMONI requires approximately 14 times longer exposure times (~10.5 hr) than ELT/METIS (0.75 hr) to achieve S/N = 5 (see Table 4).

For other planets, the S/N of ELT/HARMONI is estimated to be approximately 0.22–3.71 times that of ELT/METIS, for an exposure time of 10 hr.

Our results demonstrate that ELT/HARMONI possesses S/Ns for all four biosignatures (H_2O, CO_2, CH_4, and O_2). The S/N of H_2O is the highest, while the S/N of O_2 is the lowest.

For different instrument contrast, from $C = 10^{-2}$ to 10^{-3}, 10^{-3} to 10^{-4}, and 10^{-4} to 10^{-5}, the S/N of ELT/HARMONI for GJ 887 b improves by 216.7%, 216.2%, and 215.6%, respectively. The enhancement of instrument contrast will greatly improve the S/N of ELT/HARMONI. In the wavelength (0.47–2.45 μm) relevant to ELT/HARMONI, the noise is mainly from the host star. Such noise can be mitigated by improving the performance of the coronagraph. The setting of the contrast range is akin to that for ELT/METIS but with a different baseline contrast (from 10^{-4} to 10^{-3}; see Table 5).

5. Discussion

5.1. ELT versus JWST

Batalha & Line (2017) noted that the launch of JWST will revolutionize our understanding of planetary atmospheres. We compare the direct imaging of ELT with JWST's transit spectroscopy. Our results indicate that for those planets with small angular separation and high contrast, JWST's transit spectroscopy may exhibit better performance compared to the direct imaging methods of ELT and JWST. Below, we present these discussions in more detail.

5.1.1. ELT Direct Imaging versus JWST Transit Spectroscopy

The transit spectroscopy of JWST is another method to explore exoplanet atmospheres. Greene et al. (2016) highlighted its favorable performance in probing exoplanet atmospheres in 1–2.5 μm, which may compensate for the limitations of ELT direct imaging in this band.

For comparison, we simulated and quantified the S/N of ELT's direct imaging mode and JWST's transit spectroscopy for the same targets—TRAPPIST-1 e and h, two planets in the TRAPPIST-1 system with medium to largest angular separation among all TRAPPIST planets. TRAPPIST-1 e and h have angular separations of 2.42 and 5.11 mas, respectively, which are smaller than the minimum spatial resolution of ELT/METIS (15.74 mas); we therefore do not consider ELT/METIS in the TRAPPIST-1 discussion. The results are presented in Table 6. Based on the table, we observe that JWST's transit spectroscopy exhibits superior S/N for the atmospheres of high-contrast, low-separation planets like those in the TRAPPIST-1 system compared to ELT's direct imaging.

Table 6
The S/N of Biosignatures in the Atmospheres of TRAPPIST-1 e and h with ELT/HARMONI Direct Imaging and JWST Transit Spectroscopy

Telescope	Planet	H_2O	CH_4	CO_2	O_2	S/N$_{total}$
JWST/NIRSpec	TRAPPIST-1 e	34.85 ± 2.02	20.13 ± 2.19	16.86 ± 1.01	5.71 ± 0.95	44.04 ± 2.80
JWST/NIRSpec	TRAPPIST-1 h	35.30 ± 2.16	21.20 ± 1.78	17.30 ± 1.23	5.97 ± 1.17	45.09 ± 2.85
ELT/HARMONI	TRAPPIST-1 e	0.000	0.000	0.000	0.000	0.000
ELT/HARMONI	TRAPPIST-1 h	0.001	0.000	0.000	0.000	0.001

For the simulation of ELT direct imaging of TRAPPIST-1 e and h, we utilized the methodology describe in Section 3.

For JWST, we employed PICASO (Batalha et al. 2019) to model the planet's transmission spectra, assuming a modern Earth atmosphere (Cox 2000). Based on the obtained transmission spectra, we simulated JWST/NIRSpec (0.6–5.3 μm; Bagnasco et al. 2007) observations using PandExo (Batalha et al. 2017). For the observation strategy settings for PandExo, we set the saturation level equal to 80 (in percent); the number of transits is 10, the noise floor is 0, and R(Resolution) = 150. The settings for PandExo were consistent with the strategy outlined in Mikal-Evans (2022). To make sure we used the same setting, we reproduced the results in Mikal-Evans (2022). Using the observational results, we quantified the S/N of JWST transit spectroscopy for planetary atmospheres using the method described in Phillips et al. (2021). The result of a detection of S/N ~ 5 for O_2 in 10 transits is consistent with previous studies that concluded O_2 can be detected for 7–40 transits with JWST (Lustig-Yaeger et al. 2019; Gialluca et al. 2021).

The parameters for TRAPPIST-1 e and h are described in Table 2. The selection of the TRAPPIST-1 system was motivated by its proximity and the presence of one of the closest known terrestrial planets in transit.

5.2. ELT: The Performance of Different Detection Methods

The ELT will greatly enhance our understanding of exoplanet atmospheres in multiple aspects. Currie et al. (2023) explored the S/N of ELT's high-resolution transit spectroscopy for exoplanet atmospheres, noting that the high-resolution transit spectroscopy of ELT exhibits a strong S/N for O_2, CH_4, and CO_2 in transiting planets. High-resolution transit spectroscopy appears suitable for the detection of O_2 in exoplanets with transit phenomena (Serindag & Snellen 2019). However, Hardegree-Ullman et al. (2023) pointed out that ELT's transit spectroscopy requires about 16–55 yr to detect O_2 on TRAPPIST-1 d–g.

Our results indicate that ELT/HARMONI's ability to detect O_2 through direct imaging depends on the instrument contrast. The S/N will increase by approximately 30 times from 0.3 to 10, when the contrast (C) improves from 10^{-2} to 10^{-5}.

In addition to O_2, our findings also indicate that ELT/METIS exhibits strong S/N for CH_4, assuming instrument contrast $C = 10^{-4}$. In general, direct imaging is an important method for exploring nearby rocky planet atmospheres, as it does not rely on transits, which are extremely rare (with only one exception, HD 219134 b) for nearby (<12 pc) rocky planets.

Furthermore, the performance of ELT in the high spectral resolution direct imaging mode can be improved more for low-noise detectors, reducing the contrast requirements for planets by 2–3 orders of magnitude under high-dispersion conditions (Wang et al. 2017).

5.3. S/N of Biosignature Pairs

The presence of gases in specific combinations is related to thermal-dynamical imbalance between them, rather than a single molecule (e.g., CO_2 in the biosignature pair of CH_4 + CO_2). The high S/N of a single molecule alone does not necessarily prove the high S/N of disequilibrium phenomena. Therefore, the S/N of disequilibrium pairs composed of multiple molecules is a topic worth exploring.

We propose a quantitative approach to characterize the S/N of thermal-dynamical imbalance pairs. It takes into account the number of molecules involved in the composition of the disequilibrium pair and their S/N, as follows:

$$S/N_{total} = \left(\prod_{i=1}^{n} S/N_{gas\ i} \right)^{\frac{1}{n}}, \qquad (11)$$

where S/N$_{gas\ i}$ is the S/N of a single gas.

As an example, according to Table 6, TRAPPIST-1 e under JWST observation has an S/N of 44.04. However, the low S/N of O_2 (S/N = 5.71) will limit the detection of the biosignature pair of O_2 + CH_4.

5.4. Fidelity of the Calculations

Assumptions such as instrument sensitivity, telluric uncertainty, and the usage of feature wavelengths in this paper will lead to differences in the calculations. Below, we detail the impact of each assumption on our calculations. As shown below, our calculations provide a conservative estimate for S/N and exposure times.

Considering telluric variability as a source of noise may impact S/N, we explored two cases for telluric residual removal at 0.1% and 1% levels. The results are reported in Tables 4 and 7 for the two cases. The results indicate that telluric variability has a limited impact on ELT/HARMONI and ELT/METIS. This is reasonable, as its influence is only related to the planetary photon noise ($\frac{N_p \cdot \sigma_{f_{tran}}}{f_{tran}}$) in the noise calculations (Equation (8)), and the planetary photon noise does not dominate the noise budget.

In terms of the impact of instrumental curves (instrument throughput and coronagraph contrast) on the calculations, a higher throughput and contrast generally result in a higher S/N. The improvement in S/N due to increased throughput roughly follows a square-root law. We have assumed an instrumental throughput of 0.1 for both ELT/HARMONI and MELT/ETIS, which is a conservative assumption. The actual throughput varies with different observation modes and working wavelengths, but it is generally higher than 0.1 (Carlotti et al. 2022).

The gains in S/N due to improvements in coronagraph contrast diminish gradually as the thermal emission begins to dominate the noise budget. For instance, the working wavelength of ELT/METIS determines that it is more affected by atmospheric thermal noise; therefore, the improvement effect on S/N

Table 7
Biosignature S/N for Candidate Planets with ELT/HARMONI and ELT/METIS Direct Imaging

		ELT/METIS				
Rank	Planet	S/N_{total}	S/N_{H_2O}	S/N_{CH_4}	S/N_{CO_2}	S/N_{O_2}	$T_{S/N=5}$(hr)
1	GJ 887 b	18.16	4.80	17.52	0.00	0.0	0.75
2	Proxima b	2.22	1.57	1.16	1.05	0.0	51
3	Wolf 1061 c	0.71	0.24	0.67	0.00	0.0	490
4	GJ 682 b	0.13	0.13	0.00	0.00	0.0	14,850
5	GJ 667 C c	0.07	0.07	0.00	0.00	0.0	55,000

		ELT/HARMONI				
Rank	S/N	S/N_{total}	S/N_{H_2O}	S/N_{CH_4}	S/N_{CO_2}	S/N_{O_2}	$T_{S/N=5}$(hr)
1	GJ 887 b	4.94	3.17	2.74	2.40	1.02	10.5
2	Wolf 1061 b	1.04	0.94	0.12	0.20	0.37	235
3	Wolf 1061 c	0.64	0.43	0.34	0.29	0.13	625
4	Proxima b	0.49	0.38	0.23	0.19	0.09	1050
5	GJ 682 b	0.47	0.36	0.23	0.19	0.09	1150
6	GJ 1061 c	0.44	0.41	0.09	0.06	0.11	1300
7	GJ 667 C c	0.26	0.17	0.14	0.12	0.05	3800
8	GJ 1061 d	0.25	0.19	0.12	0.10	0.05	4000
9	GJ 1002 b	0.13	0.12	0.03	0.02	0.03	14,500
10	GJ 1002 c	0.08	0.06	0.04	0.03	0.01	39,000

Note. $T_{S/N=5}$(s): required exposure time to reach an S/N_{total} of 5. We assume an exposure time of 10 hr and a resolution of 1000 for ELT and a coronagraph contrast of 10^{-3} for ELT/HARMONI and 10^{-4} for ELT/METIS, and the uncertainty of sky transmission ($\sigma_{f_{tran}}$) equals $0.01 \cdot f_{tran}$.

diminishes progressively from contrasts of 10^{-3} to 10^{-6} and only 21.3% enhancement from 10^{-5} to 10^{-6}. ELT/HARMONI, with working wavelengths of 0.45–2.5 μm, avoids the high atmospheric thermal noise regions and demonstrates an increase of over 200% in S/N across all four explored cases from 10^{-2} to 10^{-5} (see Table 5).

Another source of uncertainty is the selection of gas feature wavelengths; we have ignored regions where the gas albedo is below 0.15, leading to an underestimation of the gas S/N. However, the method we employed still includes the majority of absorption features of the gases. The ignored regions constitute approximately 23% of the total absorption signal. The weak and blended features that are ignored in this work can be better recovered by spectral retrievals (e.g., Ruffio et al. 2023; Wang 2023). This will be the main focus of the next phase of this project.

6. Summary

We evaluated 10 and 5 rocky planets with ELT/HARMONI and ELT/METIS, respectively. We simulated high-contrast, medium-resolution ($R = 1000$) direct imaging of these planets with ELT/METIS and ELT/HARMONI in 3–5.6 and 0.5–2.45 μm. We investigated and quantified the S/N of ELT/METIS and ELT/HARMONI for the atmospheres and potential biosignatures therein. We drew conclusions with ELT and compared them with JWST. Here are our primary findings.

1. We find that the direct imaging mode of ELT/METIS has the capability to detect CH_4, CO_2, and H_2O in 3–5.6 μm. The direct imaging mode of ELT/HARMONI has the ability to detect CH_4, CO_2, O_2, and H_2O, but it requires more exposure time, especially for O_2. The direct imaging mode of ELT/METIS performs better for three planets (GJ 887 b, Proxima b, and Wolf 1061 c) with higher S/N than ELT/HARMONI. ELT/HARMONI

performs better for planets other than GJ 887 b, Proxima b, and Wolf 1061 c (see Sections 4.1 and 4.2).

2. We investigate the impact of coronagraph performance on the S/N. We find that once the instrument contrast C exceeds 10^{-5}, improvement in the coronagraph performance is less helpful for the S/N of ELT/METIS because the thermal emission begins to dominate the noise budget. From $C = 10^{-2}$ to 10^{-5}, the improvement in performance of the coronagraph greatly aids the S/N of ELT/HARMONI (see Sections 4.1 and 4.2).

3. GJ 887 b is currently the most amenable target for direct imaging with ELT, as it has a bright host star, close orbit, and large size, which result in the highest S/N (see Sections 4.1 and 4.2 and Table 4).

4. Proxima Cen b is a unique target for direct imaging with ELT/METIS, not only because it can achieve an S/N of 5 within 51 hr but also because its angular separation enables the direct observation of CO_2, H_2O, and CH_4 (see Section 4.1 and Table 4).

5. We find that for transiting planets with high contrast and small separation, such as the TRAPPIST-1 system, JWST transit spectroscopy is more suitable than ELT direct imaging in terms of the achievable detection S/N (see Section 5).

Appendix A
Derivation of Equation (8)

The photons received at the detector (N_{det}) consist of stellar photons (N_s) and planetary photons (N_p) transmitted through Earth's atmosphere (f_{tran}) and the instrument's coronagraph (C), as well as photons from the background sky radiance (N_{sky}):

$$N_{det} = N_p \cdot f_{tran} + N_s \cdot f_{tran} \cdot C + N_{sky}, \quad (A1)$$

with a photon noise of $\sqrt{N_{det}}$:

$$\sigma_{N_{det}} = \sqrt{N_p \cdot f_{tran} + N_s \cdot f_{tran} \cdot C + N_{sky}}. \quad (A2)$$

To find N_p, we could remove the stellar and background sky photons through additional observations (N_{add}), which consist of stellar photons (N_s) processed by the sky (f_{tran}) and coronagraph (C), as well as photons from the sky (N_{sky}), with a photon noise of $\sqrt{N_{add}}$.

That is,

$$N_{add} = N_s \cdot f_{tran} \cdot C + N_{sky}, \quad (A3)$$

with photon noise

$$\sigma_{N_{add}} = \sqrt{N_s \cdot f_{tran} \cdot C + N_{sky}}. \quad (A4)$$

We can compute the planetary signal transmitted through the atmosphere ($N_p \cdot f_{tran}$) by subtracting N_{add} from N_{det},

$$N_p \cdot f_{tran} = N_{det} - N_{add} = \Delta N, \quad (A5)$$

with photon noise

$$\sigma_{N_p \cdot f_{tran}} = \sqrt{\sigma_{N_{det}}^2 + \sigma_{N_{add}}^2} = \sigma_{\Delta N}. \quad (A6)$$

We remove the sky transmission (f_{tran}) through observations of a telluric standard star and divide by this signal:

$$N_p = \frac{N_{det} - N_{add}}{f_{tran}} = \frac{\Delta N}{f_{tran}}, \quad (A7)$$

with photon noise (propagation of uncertainty; Taylor 1997)

$$\frac{\sigma_{N_p}^2}{N_p^2} = \frac{\sigma_{\Delta N}^2}{\Delta N^2} + \frac{\sigma_{f_{tran}}^2}{f_{tran}^2}, \quad (A8)$$

so the final noise (σ_{N_p}) is

$$\sigma_{N_p} = \sqrt{\frac{\sigma_{\Delta N}^2}{\Delta N^2} \cdot N_p^2 + \frac{\sigma_{f_{tran}}^2}{f_{tran}^2} \cdot N_p^2}. \quad (A9)$$

Note that $\Delta N = N_p \cdot f_{tran}$, and $\sigma_{f_{tran}} = 0.001 \cdot f_{tran}$, which implies

$$\sigma_{N_p} = \sqrt{\frac{\sigma_{\Delta N}^2}{f_{tran}^2} + \left(\frac{N_p \cdot \sigma_{f_{tran}}}{f_{tran}}\right)^2}, \quad (A10)$$

and $\sigma_{\Delta N} = \sqrt{\sigma_{N_{det}}^2 + \sigma_{N_{add}}^2} = \sqrt{N_{det} + N_{add}}$, which means

$$\sigma_{N_p} = \sqrt{\frac{N_{det} + N_{add}}{f_{tran}^2} + \left(\frac{N_p \cdot \sigma_{f_{tran}}}{f_{tran}}\right)^2}, \quad (A11)$$

or

$$\sigma_{N_p} = \sqrt{\left(\frac{N_p \cdot \sigma_{f_{tran}}}{f_{tran}}\right)^2 + \frac{N_{det} + N_\star \cdot C \cdot f_{tran} + N_{sky}}{f_{tran}^2}}. \quad (A12)$$

ORCID iDs

Huihao Zhang ● https://orcid.org/0009-0006-9777-3051
Ji Wang (王吉) ● https://orcid.org/0000-0002-4361-8885
Michael K. Plummer ● https://orcid.org/0000-0002-4831-0329

References

Allard, F. 2014, in IAU Symp. 299, Exploring the Formation and Evolution of Planetary Systems, ed. M. Booth, B. C. Matthews, & J. R. Graham (Cambridge: Cambridge Univ. Press), 271
Bagnasco, G., Kolm, M., Ferruit, P., et al. 2007, Proc. SPIE, 6692, 66920M
Batalha, N. E., & Line, M. R. 2017, AJ, 153, 151
Batalha, N. E., Mandell, A., Pontoppidan, K., et al. 2017, PASP, 129, 064501
Batalha, N. E., Marley, M. S., Lewis, N. K., & Fortney, J. J. 2019, ApJ, 878, 70
Boccaletti, A. 2018, EPSC, 12, EPSC2018–778
Bowens, R., Meyer, M. R., Delacroix, C., et al. 2021, A&A, 653, A8
Brandl, B. R., Absil, O., Agócs, T., et al. 2018, Proc. SPIE, 10702, 107021U
Brandl, B. R., Agócs, T., Aitink-Kroes, G., et al. 2016, Proc. SPIE, 9908, 990820
Brandl, B. R., Lenzen, R., Pantin, E., et al. 2008, Proc. SPIE, 7014, 70141N
Carlomagno, B., Absil, O., Kenworthy, M., et al. 2016, Proc. SPIE, 9909, 990973
Carlomagno, B., Delacroix, C., Absil, O., et al. 2020, JATIS, 6, 035005
Carlotti, A., Jocou, L., Moulin, T., et al. 2022, Proc. SPIE, 12185, 121855L
Charbonneau, D., Brown, T. M., Noyes, R. W., & Gilliland, R. L. 2002, ApJ, 568, 377
Chauvin, G., Desidera, S., Lagrange, A. M., et al. 2017, A&A, 605, L9
Chen, J., & Kipping, D. 2017, ApJ, 834, 17
Cox, A. N. 2000, Allen's Astrophysical Quantities (4th edn.; New York: Springer)
Crouse, J., Bastelberger, S., Arney, G. N., et al. 2021, BAAS, 53, 0202
Currie, M. H., Meadows, V. S., & Rasmussen, K. C. 2023, PSJ, 4, 83
Davies, R., Ageorges, N., Barl, L., et al. 2010, Proc. SPIE, 7735, 77352A
Deming, D., Wilkins, A., McCullough, P., et al. 2013, ApJ, 774, 95
Des Marais, D. J., Harwit, M. O., Jucks, K. W., et al. 2002, AsBio, 2, 153
Fortney, J. J., Marley, M. S., Saumon, D., & Lodders, K. 2008, ApJ, 683, 1104
Gialluca, M. T., Robinson, T. D., Rugheimer, S., & Wunderlich, F. 2021, PASP, 133, 054401
Gilmozzi, R., & Spyromilio, J. 2007, Msngr, 127, 11
Ginzburg, S., Schlichting, H. E., & Sari, R. 2016, ApJ, 825, 29
Ginzburg, S., Schlichting, H. E., & Sari, R. 2018, MNRAS, 476, 759
Goode, P. R., Qiu, J., Yurchyshyn, V., et al. 2001, GeoRL, 28, 1671
Greene, T. P., Line, M. R., Montero, C., et al. 2016, ApJ, 817, 17
Gupta, A., Nicholson, L., & Schlichting, H. E. 2022, MNRAS, 516, 4585
Gupta, A., & Schlichting, H. E. 2019, MNRAS, 487, 24
Haghighipour, N. 2013, AREPS, 41, 469
Hardegree-Ullman, K. K., Apai, D., Bergsten, G. J., Pascucci, I., & López-Morales, M. 2023, AJ, 165, 267
Houllé, M., Vigan, A., Carlotti, A., et al. 2021, A&A, 652, A67
Hu, R., Ehlmann, B. L., & Seager, S. 2012a, ApJ, 752, 7
Hu, R., & Seager, S. 2014, ApJ, 784, 63
Hu, R., Seager, S., & Bains, W. 2012b, ApJ, 761, 166

Hu, R., Seager, S., & Bains, W. 2013, ApJ, 769, 6
Huang, J., Seager, S., Petkowski, J. J., Ranjan, S., & Zhan, Z. 2022, AsBio, 22, 171
Jeffers, S. V., Dreizler, S., Barnes, J. R., et al. 2020, Sci, 368, 1477
Jocou, L., Rabou, P., Moulin, T., et al. 2022, Proc. SPIE, 12185, 121854K
Johns, M. 2006, Proc. SPIE, 6267, 626729
Jones, A., Noll, S., Kausch, W., Szyszka, C., & Kimeswenger, S. 2013, A&A, 560, A91
JWST Transiting Exoplanet Community Early Release Science Team, Ahrer, E.-M., Alderson, L., et al. 2023, Natur, 614, 649
Kasper, M., Arsenault, R., Käufl, H. U., et al. 2017, Msngr, 169, 16
Kenworthy, M. A., Absil, O., Agócs, T., et al. 2016, Proc. SPIE, 9908, 9908A6
Kosmalski, J., Tecza, M., Bryson, I., et al. 2016, Proc. SPIE, 9908, 99089T
Krissansen-Totton, J., Olson, S., & Catling, D. C. 2018, SciA, 4, eaao5747
Lagrange, A. M., Bonnefoy, M., Chauvin, G., et al. 2010, Sci, 329, 57
Lustig-Yaeger, J., Meadows, V. S., & Lincowski, A. P. 2019, AJ, 158, 27
Macintosh, B., Graham, J. R., Barman, T., et al. 2015, Sci, 350, 64
Mâlin, M., Boccaletti, A., Charnay, B., Kiefer, F., & Bézard, B. 2023, A&A, 671, A109
Marois, C., Macintosh, B., Barman, T., et al. 2008, Sci, 322, 1348
Marois, C., Zuckerman, B., Konopacky, Q. M., Macintosh, B., & Barman, T. 2010, Natur, 468, 1080
Mawet, D., Fitzgerald, M. P., Konopacky, Q., et al. 2022, Proc. SPIE, 12184, 121841R
Mikal-Evans, T. 2022, MNRAS, 510, 980
Miller-Ricci, E., Seager, S., & Sasselov, D. 2009, ApJ, 690, 1056
Noll, S., Kausch, W., Barden, M., et al. 2012, A&A, 543, A92
Owen, J. E., & Schlichting, H. E. 2023, arXiv:2308.00020
Owen, J. E., & Wu, Y. 2017, ApJ, 847, 29
Phillips, C., Wang, J., Edwards, B., et al. 2023, MNRAS, 526, 2251

Phillips, C. L., Wang, J., Kendrew, S., et al. 2021, ApJ, 923, 144
Quanz, S. P., Crossfield, I., Meyer, M. R., Schmalzl, E., & Held, J. 2015, IJAsB, 14, 279
Rameau, J., Chauvin, G., Lagrange, A. M., et al. 2013, ApJL, 779, L26
Roberge, A., & Moustakas, L. A. 2018, NatAs, 2, 605
Ruffio, J.-B., Perrin, M. D., Hoch, K. K. W., et al. 2023, arXiv:2310.09902
Sanders, G. H. 2013, JApA, 34, 81
Schwieterman, E. W., Kiang, N. Y., Parenteau, M. N., et al. 2018, AsBio, 18, 663
Seager, S. 2013, Sci, 340, 577
Selsis, F., Kasting, J. F., Levrard, B., et al. 2007, A&A, 476, 1373
Serindag, D. B., & Snellen, I. A. G. 2019, ApJL, 871, L7
Sharp, R., Bloxham, G., Boz, R., et al. 2016, Proc. SPIE, 9908, 99081Y
Stüeken, E. E., Som, S. M., Claire, M., et al. 2020, SSRv, 216, 31
Tamai, R., Cirasuolo, M., González, J. C., Koehler, B., & Tuti, M. 2016, Proc. SPIE, 9906, 99060W
Taylor, J. 1997, Introduction to Error Analysis, the Study of Uncertainties in Physical Measurements (2nd edn.; Herndon, VA: Univ. Science Books)
Thatte, N. A., Clarke, F., Bryson, I., et al. 2016, Proc. SPIE, 9908, 99081X
The National Academies of Sciences Engineering Medicine 2021, Pathways to Discovery in Astronomy and Astrophysics for the 2020s, doi:10.17226/26141
Wang, J. 2023, AJ, 166, 203
Wang, J., & Jurgenson, C. 2020, AJ, 160, 210
Wang, J., Mawet, D., Ruane, G., Hu, R., & Benneke, B. 2017, AJ, 153, 183
Wenger, M., Ochsenbein, F., Egret, D., et al. 2000, A&AS, 143, 9
Werber, Z., Wagner, K., & Apai, D. 2023, AJ, 165, 133
Wogan, N., Krissansen-Totton, J., & Catling, D. C. 2020, PSJ, 1, 58
Zhang, H. 2023, E-ELT-snr, v2.0, Zenodo, doi:10.5281/zenodo.10075564